Journal of Nuclear Materials 512 (2018) 46–55

Contents lists available at ScienceDirect

Journal of Nuclear Materials

journal homepage: www.elsevier.com/locate/jnucmat

Cracking and spalling of the oxide layer developed in high-burnup Zircaloy-4 cladding under normal operating conditions in a PWR

Kisik Hong [a], J.R. Barber [a], M.D. Thouless [a, b], Wei Lu [a, *]

[a] Department of Mechanical Engineering, University of Michigan, Ann Arbor, MI, 48109, USA
[b] Department of Materials Science & Engineering, University of Michigan, Ann Arbor, MI, 48109, USA

HIGHLIGHTS

- Model of crack evolution in the oxide layer of cladding and oxide spalling.
- Outer region of oxide layer becomes tensile after a critical oxide thickness.
- Newly formed oxide induces a tensile contribution to the oxide formed earlier.
- Three types of crack may form depending on oxide thickness and toughness.
- A radial crack may channel; spall depth is typically smaller than oxide thickness.

GRAPHICAL ABSTRACT

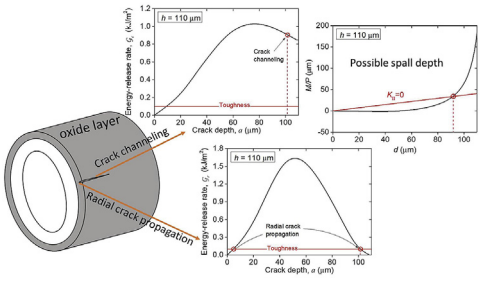

ARTICLE INFO

Article history:
Received 25 April 2018
Received in revised form
1 October 2018
Accepted 2 October 2018
Available online 3 October 2018

ABSTRACT

In this paper, the evolution of cracks from the surface of a thick oxide layer on Zircaloy-4 cladding has been analyzed for the normal operation of pressurized-water reactors. The conditions for the propagation of radial cracks towards the interface, channeling along the axis of the cladding, and the possible subsequent spalling of the oxide have been studied. The analysis was conducted by first calculating how the stresses in the oxide developed during operation, using a numerical model that incorporates multiple mechanisms such as creep, swelling and oxidation. These calculations demonstrate that the circumferential stresses within the oxide increase as oxidation proceeds and as the cladding expands under the effect of fuel swelling. Although the intrinsic growth stresses of the oxide are compressive, tensile stresses can eventually develop in the outer region of the oxide. Within this regime, the energy-release rate for the radial propagation of a crack was determined using the *J*-integral along with the calculated stress profile. By assuming a suitable value of toughness for the oxide, it is possible to determine the depth to which such a radial crack can grow. A second fracture-mechanics calculation was then conducted to explore the conditions under which such a surface crack can subsequently channel along the axial direction of the cladding. A third fracture-mechanics analysis considered oxide spalling. This showed the possibility of spalling from the radial cracks, which leaves a thin layer of the oxide adhered to the metal that can result in a local cold spot responsible for hydride formation.

1. Introduction

The exterior surfaces of fuel rods are exposed to the primary coolant during operation of a pressurized-water reactor (PWR).

* Corresponding author.
E-mail address: weilu@umich.edu (W. Lu).

https://doi.org/10.1016/j.jnucmat.2018.10.003
0022-3115/

This results in oxidation of the Zircaloy cladding. A complementary process to oxidation is the formation of hydrogen, which in some cases can diffuse into the Zircaloy and form brittle hydrides. These hydrides tend to precipitate in the colder regions of the cladding [1]. Since the oxide layer serves as a thermal barrier against the coolant, local cold spots are formed where hydrides may precipitate [2] if the integrity of the oxide is compromised by cracking or spalling. Since the ductility of Zircaloy decreases dramatically with an increase in hydride concentration [3,4], the spalled area can become vulnerable to what is termed pellet-cladding-interaction [5] failure. The intent of this study is to explore the mechanics of how an oxide layer might crack and spall as a result of mechanical interaction between the pellet and cladding during normal operation of a reactor. It is important to appreciate that this is a study of the radial cracks and spalls that can develop when the oxide is thick. It is not a study of the defects that appear to align parallel to the interface during early stages of oxidation, which are sometimes equated to cracks (despite the absence of significant radial tensile stresses or obvious signs of buckling).

An insight into the process is given by the results of the CABRI REP-Na program, performed by the French Institut de Radioprotection et de Súretè Nucléaire (IRSN) in the early 90's to study what is termed a reactivity-initiated accident (RIA) with irradiated fuel rods [6–9]. An RIA corresponds to a rapid power transient in a fuel rod over a few milliseconds. This leads to extreme thermal expansion together with fission-gas-induced swelling of the fuel pellet, and a strong interaction between the pellet and cladding that can result in oxide spalling. Various efforts have been made to improve the understanding of oxide spalling during an RIA. For instance, studies were conducted to analyze the phenomenon, based on metallographic investigations of the CABRI REP-Na test rods that exhibited spalling [10,11]. Cracking of the oxide layer was explained by implementing a shear-lag model, with a tensile circumferential stress being generated in the cladding and oxide layer because of the thermal expansion and swelling of the pellet against the cladding, and being transferred to the oxide layer. Also, finite-element calculations were performed by assuming a partially fragmented oxide layer, with further fragmentation being assumed to occur during the power transient when the circumferential stress in the oxide reached an assumed critical value.

These previous analyses concentrated on the cracking and spalling of the oxide layer during a transient power spike. The simulations were conducted with pre-oxidized claddings, and the characteristics of the oxide layer that can form on fuel rods during long service in a reactor were neglected. However, the stress in the oxide layers of heavily corroded fuel rods can be quite significant, and spalling was observed under normal operating conditions on some test rods consisting of standard Zircaloy-4 (1.5% Sn) cladding and UO_2 fuel before being subjected to the RIA transient [8].

It is the possible development of stresses and the subsequent crack evolution in the oxide layer under normal operating conditions, rather than spalling under an RIA transit, that is studied in the present paper. The model we present incorporates essential mechanisms such as creep, swelling, and oxidation into a finite-element simulation. A cracking analysis is performed, based on the stress distribution that is obtained from the model. In contrast to previous analyses that invoked the concept of a fracture strength for a brittle material, we implement a more rigorous fracture-mechanics-based approach to describe the propagation of cracks within the oxide layer.

2. Model

The analysis of cracking in the oxide layer consists of three steps: (i) obtaining the stress state within the oxide, (ii) using this stress distribution to calculate the depth to which an incipient flaw may grow, and (iii) computing the conditions for when this flaw can channel along the oxide to form a significant crack. Therefore, three separate finite-element calculations were conducted sequentially. The first of these captured the stress evolution within the oxide layer during service, while the other two were fracture-mechanics calculations.

2.1. Development of stress in the oxide layer

2.1.1. Geometry and boundary conditions

A finite-element model for the fuel rod, including the fuel pellet and cladding, was constructed using the commercial software program, ABAQUS. As shown in Fig. 1, a simplified, axisymmetric model was implemented, based on the approximate dimensions of a fuel rod in a PWR. First-order, coupled temperature-displacement, axisymmetric elements with reduced integration were used in an implicit calculation. During the simulation, the displacement and temperature fields were solved simultaneously using nonlinear thermomechanical calculations, to ensure an appropriate relationship between them.

The displacements along the axis of the cylinder corresponding to the fuel rod (the z-direction) were constrained so that the results varied only along the radial r-direction, and the analysis was axisymmetric. An initial gap of 80 μm between the pellet and cladding was assumed to be filled with helium gas. The pressure of this internal gas was set to 4 MPa, and a pressure of 16 MPa associated with the primary coolant [12] was applied to the outer surface of the cladding. Any contact between the pellet and cladding was assumed to be axisymmetric, with a normal-hard-contact, finite-sliding, and surface-to-surface formulation. To prevent penetration between the surfaces, the direct method was used for

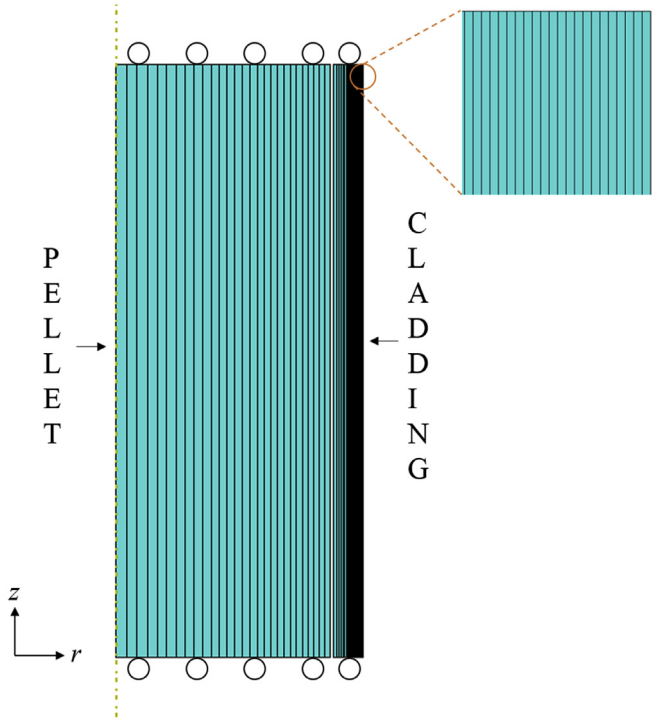

Fig. 1. A simplified axisymmetric model for the fuel rod including fuel pellet and cladding. Dimensions are implemented based on approximate values for a fuel rod in a PWR. The displacement along z-direction is constrained. There is an internal pressure between the pellet and cladding because of helium gas, and an external pressure outside of the cladding because of the primary coolant.

enforcing the constraint in the normal direction.

Thermal boundary conditions were established by assuming that the fuel rod was initially at 300 K. A uniform power generation of 20 kW/m, a typical value for a PWR [13], was applied to the fuel as a body heat flux. The temperature of the outer surface of the cladding was held at a constant value of 600 K, corresponding to the temperature of the primary coolant.

2.1.2. Model of oxidation and other deformation mechanisms

Oxidation of zirconium leads to an increase of its volume, with the ratio of the oxide volume to the corresponding metal volume (the Pilling-Bedworth ratio) being 1.56 [14]. If the unconstrained volume increase from oxidation is assumed to be isotropic, and the material behavior is assumed to be elastic, constraint by the metal substrate would result in unrealistically high in-plane compressive stresses (around 56 GPa) immediately after oxidation. Many experiments have been designed to estimate the stress in zirconium oxide layers. These have been based on curvature measurements [15], XRD [16,17], and on Raman spectroscopy [18]. The authors of these studies have reported in-plane compressive stresses in the range of 2 ±0.2 GPa at the early stage of oxidation, suggesting that yield occurs immediately after oxide formation. We therefore assume that newly formed oxide starts from a condition of an in-plane compressive stress equal to 2 GPa. In the simulation, this was achieved by assigning an appropriate initial in-plane strain to the oxide layer. The out-of-plane strain, which was associated with the dimensional change in radial direction, was assigned so as to maintain the correct Pilling-Bedworth ratio.

In the model, the area near the outer surface of the cladding was partitioned into fine elements, each of equal thickness as shown in Fig. 1. The oxidation process was incorporated into the simulation by the following steps. First, the oxide interface was assumed to advance by the thickness of one element, and the material properties of the element were changed from those of Zircaloy to those of zirconia. This was implemented into the calculation using field variables with the USDFLD subroutine. The in-plane and out-of-plane strains described above were assigned to the transformed element to mimic volume expansion of the element, using the UEXPAN subroutine. Second, creep, thermal expansion and swelling, as appropriate, of the UO_2 pellet, Zircaloy and oxide layer were implemented through the UEXPAN and CREEP subroutines. The time steps for the calculations were determined by dividing the element thickness by the oxidation rate corresponding to the current oxide thickness. The process was repeated for each subsequent layer of elements as oxidation proceeded. The appropriate thickness of the elements was determined by a mesh-sensitivity test. It was found that a mesh size of 1 μm for the particular geometry and conditions used in this study was more than adequate to ensure convergence of the stresses in the oxide to a mesh-independent value, within acceptable limits of numerical uncertainty.

Zircaloy exhibits cubic oxidation with periodic breakaway [19], resulting in an approximately constant oxidation rate [20,21]. The appropriate oxidation rate for the standard Zircaloy-4 (1.5% Sn) was estimated from experimental data [8], which indicates that the oxide grows to about 80 μm after 54 months at a burn-up level of 60 GWd/t, corresponding to a rate of 1.48 μm/month.

The creep calculations for Zircaloy-4 were based on a recent deformation-mechanism map that was developed from many decades of experimental creep data [22]. The creep parameters for UO_2 were taken from an earlier deformation-mechanism map [23]. The creep models for both Zircaloy and UO_2 incorporated multiple creep mechanisms, including dislocation creep, diffusional creep, and power-law creep. The numerical approach developed in Ref. [22] was used, whereby micromechanics models were incorporated into the FEM code, allowing all possible creep mechanism to act simultaneously, with the dominant mechanism evolving naturally as a function of local stress and temperature. Obtaining suitable parameters for the creep of zirconium oxide was more difficult owing to the lack of appropriate experimental studies. The only available experimental data appear to be for yttria-stabilized zirconia [24–26], focusing on diffusional creep at relatively high temperatures ($T > 1200$ K) and low stresses ($\sigma < 300$ MPa). Using the parameters from these studies, it appears that creep of the oxide may have a negligible effect on the evolution of stresses within it, so oxide creep was ignored in these calculations. While it is noted that this neglect of oxide creep may influence the details of the stresses in the oxide, the broader conclusions of the results presented here are not affected.

The grain sizes of the Zircaloy, UO_2 and zirconia (where needed for the creep calculations) were assumed to be 50 μm, 10 μm and 25 nm, respectively. In addition, the model for swelling of UO_2, which arises from the accumulation of fission products within the pellet, and the thermal conductivity of the helium in the gap between the pellet and cladding were taken from the MATPRO model [27]. Other parameters needed for the analysis, including the elastic properties, specific heat, density, thermal conductivity, and thermal expansion coefficients were also taken from MATPRO [27].

2.2. Analysis of the oxide fracture

2.2.1. Geometry and boundary conditions

2The geometry of the cladding corresponding to a fixed time and thickness of oxide was imported into a new model to calculate the fracture mechanics. In the geometry for this model, a radial surface crack was assumed to extend from the surface to a depth a within the oxide. It was assumed that the length of this crack along the axis of the cladding was much greater than the crack depth, so a two-dimensional model, as in Fig. 2, could be used. The calculations were performed under plane-strain conditions, with crack-tip elements and a refined mesh being used near any prospective contact areas, to improve their accuracy. The material properties were assigned fixed values appropriate for a temperature of 600 K.

Since, the calculations in this section were concerned with the energetics of brittle fracture, creep was not included in the fracture calculations. The radial distribution of circumferential stresses at the corresponding time of interest was imported from the analysis described in the previous section. This distribution was represented as a function of radial position by using a polynomial fit, and was applied as tractions (of the opposite sign) to both surfaces of the crack, using the subroutine DLOAD. Only mode-I fracture was considered since no shear stresses were developed along the plane of the crack within the oxide. This approach of representing a stress distribution by a corresponding tractions over the crack surface is a well-established technique in fracture mechanics to calculate crack-driving forces that can be used to assess the propensity of a coating or layer to fracture under residual stresses.

2.2.2. Fracture-mechanics calculations

Two distinct calculations are required to compute the conditions for crack channeling in a coating with a varying distribution of stresses. The first is to compute the depth to which a radial crack might grow perpendicular to the surface (Fig. 3a). The second is to compute whether a crack of this depth can channel along the film, parallel to the surface (Fig. 3b).

The energy-release rate for radial growth was determined by calculating the value of the J-integral for a crack with the corresponding tractions on its surface. The equilibrium depth was then computed by finding the crack depth for which the energy-release rate equals the toughness of the oxide. Once the depth to which a

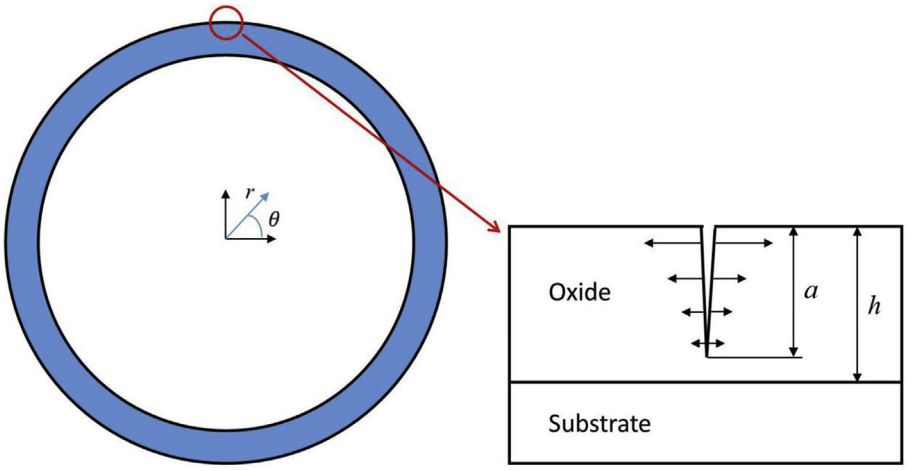

Fig. 2. A 2D model of cladding in the r-θ plane with a radial crack introduced to the oxide layer of thickness h at $\theta = 90^{\circ}$ (left). The radial crack is subjected to an internal pressure corresponding to the stress calculated from the uncracked model (right). This configuration is used to calculate the strain-energy values for the cracking analysis.

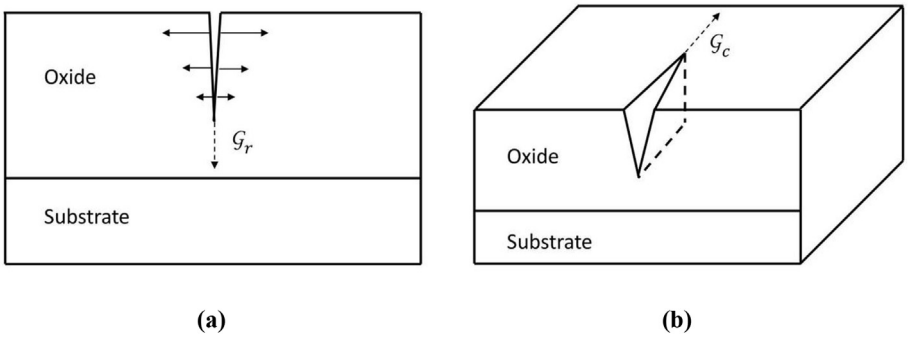

Fig. 3. The geometry considered for the crack analysis. **(a)** The propagation of a radial crack towards the metal-oxide interface **(b)** The propagation of a channeling crack in the axial direction along the oxide.

surface crack could grow in a radial direction had been established, the conditions for channeling along the length of the cladding (Fig. 3b) were computed by a second analysis. Calculations for the energy-release rate of steady-state channeling along a coating can be done by one of two approaches. One approach is to compare the elastic strain energies between an uncracked region far ahead of the channel crack (Fig. 4a) and a cracked region (Fig. 4b) far behind the crack tip [28]. An alternative, and more direct approach that we use here, is to compute the energy-release rate from the work done by the equivalent tractions on the surfaces of the crack that correspond to the circumferential stress being relaxed by the crack, as illustrated in Fig. 4c [29]. The conditions for whether channeling occurs or not can then be computed by comparing this energy-release rate to the toughness of the oxide.

Unfortunately, experimental values for the toughness of the oxide appear to be focused on the toughened structural material of yttria-stabilized zirconia [30,31], which may not be very relevant to a thermal oxide. Therefore, the results have been presented in terms of the energy-release rates. We have subsequently provided an illustrative example using an estimated value for the toughness that would be typical for a ceramic. But, it is a fairly simple exercise for a reader who may have access to more definitive data to calculate what would happen with different values of toughness. In particular, we note that the broad conclusions are not affected by the details of the toughness. The conditions for cracking, channeling and spalling are met over a relatively narrow window of oxide thickness for a broad range of toughness values.

3. Results and discussion

3.1. Development of stresses in the oxide layer

3.1.1. Contact between the fuel and cladding

During the initial assembly of a fuel rod, there is a gap of about 80 μm between the fuel pellet and the interior surface of the cladding. This gap reduces to about 46 μm immediately after the fuel rod enters service, owing to thermal expansion and the elastic effects induced by the pressure of the coolant acting on the outer surface of the cladding. During service, fission products lead to swelling of the fuel pellet, while creep leads to shrinkage of the cladding. Both of these effects cause the gap to decrease with time and, eventually, close. Further swelling of the fuel pellet then increases the contact pressure, and the pellet pushes the cladding radially outward. Under the influence of this swelling, the cladding expands by creep of the Zircaloy. It is this creep of the Zircaloy that can eventually lead to fracture of the oxide. Using the parameters and models discussed in Section 2.1, finite-element results for how the gap and contact pressure evolve with time are given in Fig. 5.

3.1.2. Stress in the oxide layer

The effect of interactions between creep, fuel swelling and oxidation can be seen in the plot of Fig. 6, which shows how the circumferential stress in the outer layer of the oxide changes as oxidation proceeds to a thickness of 100 μm. Initially, the stress in the outer layer is dominated by the compressive growth stress, and

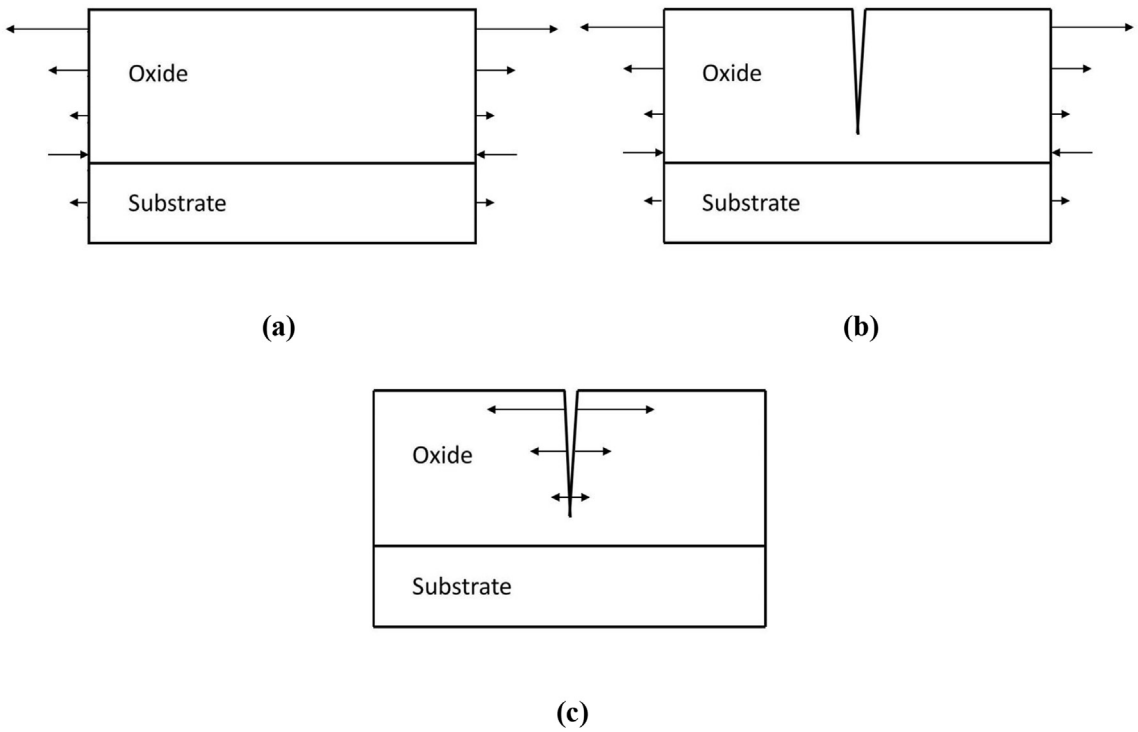

Fig. 4. The geometry considered for the crack-channeling analysis. **(a)** The configuration of an uncracked region far ahead of the channel crack. **(b)** The configuration of a cracked region. **(c)** The configuration of a crack with an internal pressure which corresponds to the stress field in the uncracked configuration. The difference in elastic energy, **(a)**–**(b)**, can be directly calculated with **(c)**.

the creep-down of the cladding increases the magnitude of the compression. However, once contact between the fuel pellet and the cladding occurs, the outwards expansion of the cladding contributes to the development of tension in the outer regions of the oxide.

Besides the above mechanisms, there are less obvious phenomena that induce changes in the stress in the outer regions of the oxide. Immediately after the fuel rod goes into service, thermal expansion increases the circumferential stress at the outer surface of the cladding, while elastic effects resulting from the external pressure reduce the stress. Since the effect of the coolant dominates over that of thermal expansion, the outermost surface of the cladding becomes slightly compressive before oxidation occurs. The increase in volume associated with the formation of new oxide at the interface with the metal forces the outer oxide layers outwards, in the radial direction. This generates circumferential tension within the outer layers. A separate calculation showed that this contribution to the accumulation of the tensile stress in the outermost layer of the oxide is about half the contribution from the fuel swelling for an oxide layer with a thickness of 100 μm. This proportion depends on how fast the oxide grows. For a high-corrosion-resistance zirconium alloy (such as low-tin zirconium alloy), where a thinner oxide develops under similar operating conditions, fuel swelling is relatively more important.

The radial distribution of the circumferential, $\sigma_{\theta\theta}$, and axial, σ_{zz}, components of the stresses is shown in Fig. 7 for a 100 μm-thick oxide layer. The circumferential stress is tensile and just under 0.5 GPa at the outmost surface of the oxide layer. This can also been

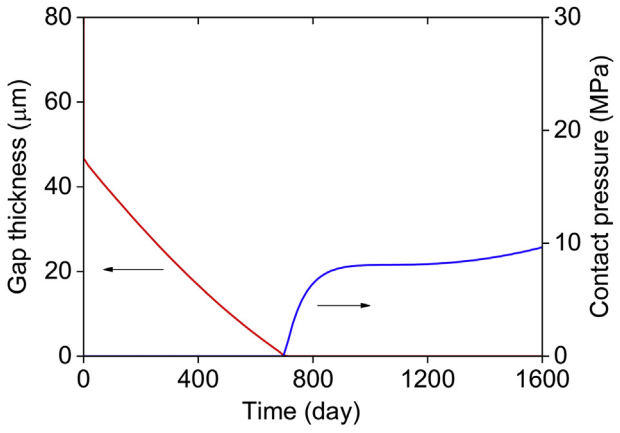

Fig. 5. Evolution of the gap thickness and contact pressure with time.

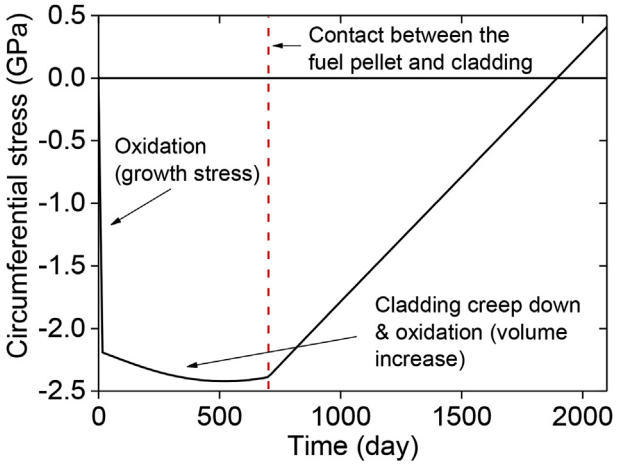

Fig. 6. Development of the circumferential stress at the outermost oxide surface with time until the oxide thickness reaches 100 μm.

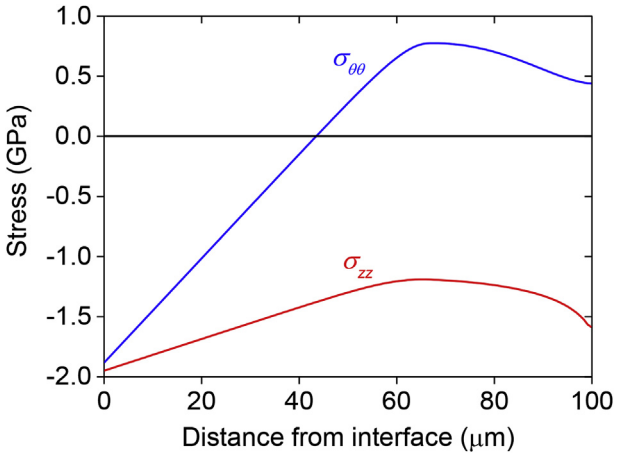

Fig. 7. Stress distribution in an oxide layer of 100 μm thickness: circumferential stress ($\sigma_{\theta\theta}$) and axial stress (σ_{zz}).

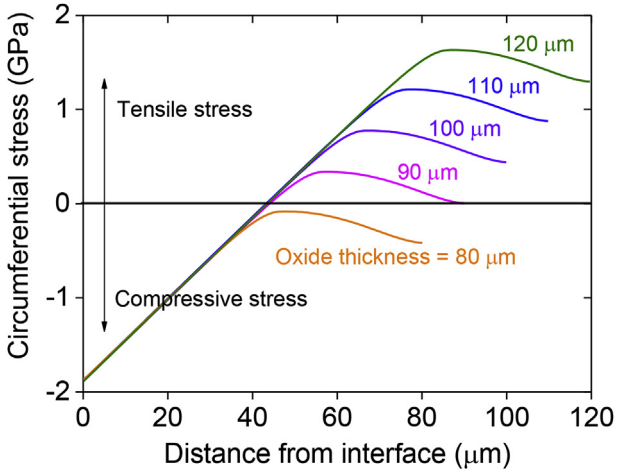

Fig. 8. Distribution of the circumferential stresses in oxide layers with different thicknesses.

seen in Fig. 6 for the corresponding length of time. Fig. 7 also illustrates the large compressive stress associated with growth at the metal-oxide interface and the transition to tension at about 40 μm away from the interface. Similar plots for how the circumferential stress varies with radial distance from the metal-oxide interface are shown in Fig. 8 for oxide thickness in the range of 80 μm–120 μm. It will be seen from this figure that if the oxide is thicker than about 80 μm, sub-surface regions of tensile stresses develop, whereas if the oxide is thicker than about 90 μm, the outer region of the oxide layer also develops tensile circumferential stresses. In even thicker oxides, the tensile stresses become quite large.

It will be shown in the following section that the tendency for the oxide film to crack increases dramatically above a critical thickness. There is a narrow range of thicknesses below which any reasonable value of oxide toughness would not lead to cracking, and above which any reasonable value of oxide toughness would lead to extensive crack channeling, multiple cracking, and spalling. It should be noted that these thicknesses correspond to a particular oxidation rate. As discussed later, the critical thicknesses become lower for lower oxidation rates.

3.2. Fracture analysis of the oxide cracking

3.2.1. Crack channeling

As described earlier, the first step in calculating the fracture mechanics of crack channeling is to compute the depth of the channel cracks. This is done by computing the depths to which a radial crack might grow in the oxide under the influence of the circumferential stresses for different oxide thicknesses. The change in potential energy available for crack growth can be computed directly from the work done by tractions (of the opposite sign to the stresses) applied to the surface of a crack. Specifically, we calculated the *J*-integral resulting from the application of the tractions, and equated this to the energy-release rate. As will be apparent from the plots of energy-release rate against crack depth (Fig. 9), the energy-release rate initially increases with crack depth, reaches a maximum, and then drops if a crack becomes deep enough to be influenced by the compressive stresses within the oxide. The smallest flaw that could propagate in a radial direction can be found from the minimum crack length for which the energy-release rate exceeds the toughness. Similarly, the depth to which a crack propagates can be found from the largest crack size for which the energy-release rate exceeds the toughness.

In these calculations, it was assumed that all the cracks extended from the surface. We did not consider the possibility of sub-surface channeling. As can be seen from Fig. 8, there is only a very narrow range of oxide thicknesses, between 80 and 90 μm, for which there is a sub-surface region of tension with compression on the surface, and for which sub-surface channeling might be expected. Plots of the energy-release rate, G_r, are shown in Fig. 9 (left) as a function of crack depth below the surface for four different thicknesses of oxide, h, corresponding to 90 μm, 100 μm, 110 μm, and 120 μm. The energy-release rates are calculated for putative cracks of any size that extend from the oxide surface ($a = 0$) to the metal interface ($a = h$). As the thickness of the oxide increases, the values of the energy-release rates increase dramatically. In particular, for oxide thickness greater than about 110 μm, the energy-release rate is positive for cracks that extend all the way to the interface. Since the modulus of the Zircaloy is less than the modulus of the oxide, one would expect a singular energy-release rate if the crack tip reaches the interface [29], so that under these conditions the crack would be drawn slightly into the metal. This effect could just be resolved with the size of mesh used in these calculations for the case of an oxide thickness of 120 μm. As an example, it is possible to see a small kink at the end of the plot for the energy-release rate (Fig. 9d (left)) for a crack depth of just less than 120 μm.

Once the depth of a radial crack has been determined, the conditions under which it might channel along the axial direction of the cladding is computed. By assuming that the crack is much longer than its depth, a steady-state energy balance can be used to compute the energy-release rate for crack channeling G_c. This is plotted in Fig. 9 (right) as functions of different crack depths. In a similar fashion to radial-crack evolution, the energy-release rate increases initially with crack depth, but decreases for deeper cracks, under the effect of the compressive stresses near the metal-oxide interface. As expected, the energy-release rate increases significantly as the oxide layer thickens. In Fig. 9a–c, the plot for the energy-release rate for crack channeling, G_c, is truncated for the depth at which the crack tip closes because of the compressive stresses.

The results of the calculations given above allow one to deduce crack depths and conditions for channeling, if the toughness of the oxide is known. Unfortunately, data for the toughness of a native-grown oxide of Zircaloy do not seem to exist in the literature. Most data for the toughness of zirconium oxide are for the partially-stabilized forms designed to have a high toughness. Therefore, owing to the lack of experimental data, we assume a toughness of 100 J/m^2, which is not unreasonable for a poly-crystalline ceramic

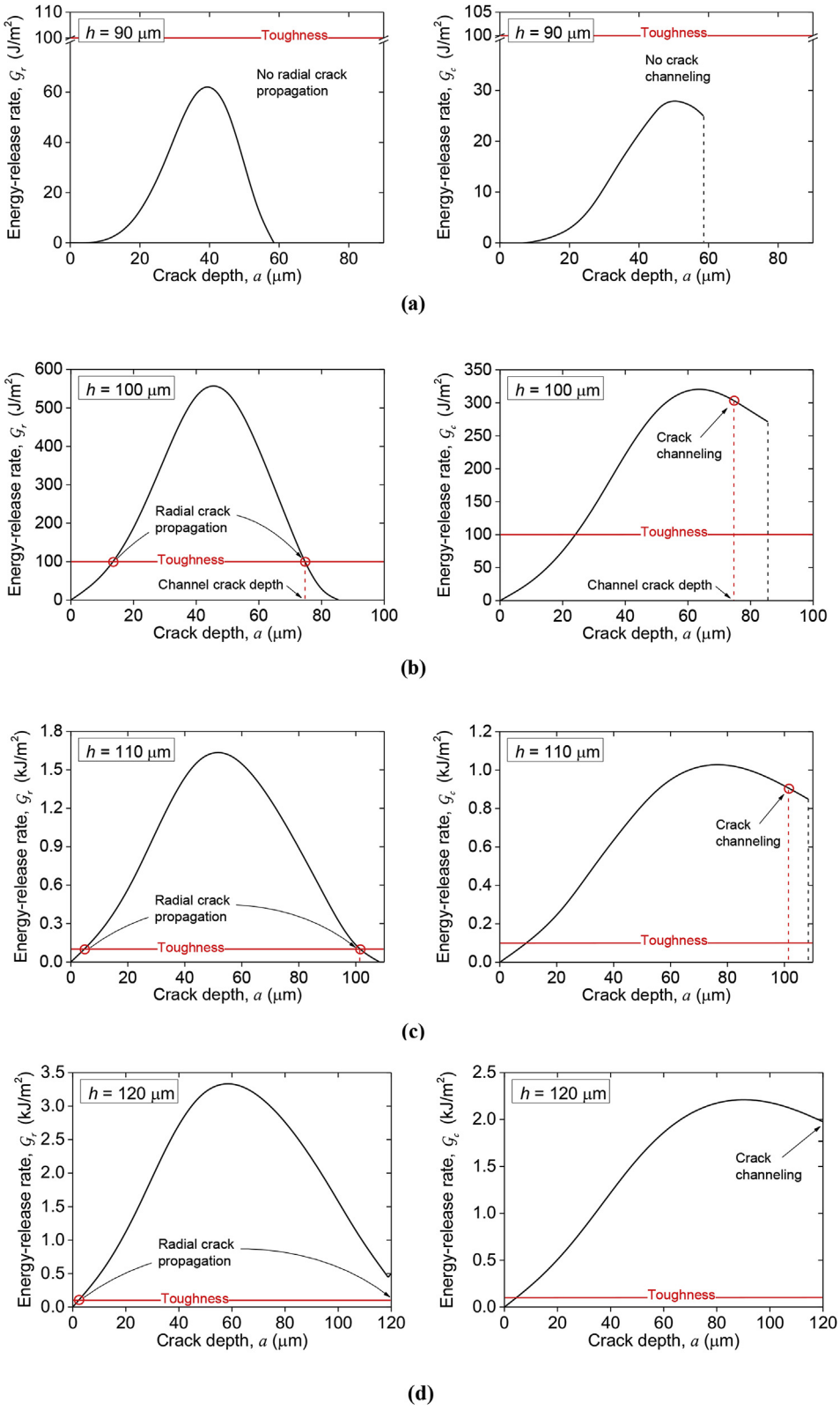

Fig. 9. Energy-release rates for a crack propagating from the surface towards the interface, to calculate the depth of a channel crack (left), steady-state energy-release rates for crack channeling (right) at different oxide thicknesses: **(a)** 90 μm, **(b)** 100 μm, **(c)** 110 μm, and **(d)** 120 μm. The horizontal line corresponds to toughness 100 J/m^2.

[32], and use this value to illustrate the behavior. With this value of toughness, no flaws can propagate within an oxide thinner than 90 μm. Provided there are initial flaws greater than about 13 μm, cracks can grow and channel to a depth of about 74 μm for a 100 μm thick oxide. Similarly, with an initial flaw size larger than about 5 μm, cracks can grow and channel to a depth of about 101 μm for a 110 μm thick oxide. For an oxide thickness of 120 μm, initial flaws deeper than 3 μm can propagate to the metal-oxide interface. These may penetrate into the substrate as discussed above, and then channel through the oxide with their tips in the cladding. As mentioned previously, the energy-release rate increases significantly with increases in the thickness of oxide layer, so different values of toughness will provide similar conclusions, although the details of the crack depths will be different. Not considered in this analysis is what happens when the energy-release rate for channeling becomes sufficiently large for multiple channels to propagate [33–36], as observed in the cross-section metallography of CABRI REP-Na test rods [10].

3.2.2. Spalling analysis

A radial crack propagating down through a layer under residual tension can kink and propagate parallel to the interface, causing spalling [37]. The depth at which this spalling will occur can be determined by finding the depth at which the crack-tip phase angle of a circumferential crack originating from a radial crack is zero [37]. The phase angle can be expressed as $\psi = \tan^{-1}(K_{II}/K_I)$, where K_I and K_{II} are the mode-I and mode-II stress-intensity factors, respectively. A mode-II component of the stress-intensity factor will tend to drive the crack out of the plane in which it is propagating. Therefore, by finding the depth at which the phase angle is zero, the depth of the steady-state trajectory can be found [37].

The effects of the tractions required to relax the circumferential stresses, $\sigma_{\theta\theta}$, that act on the surface of the radial crack can be expressed in terms of an equivalent load, P, and an equivalent moment, M (Fig. 10a):

$$P = \int_{h-d}^{h} \sigma_{\theta\theta} dr \tag{1}$$

$$M = \int_{h-d}^{h} (\sigma_{\theta\theta} - P/d) r dr \tag{2}$$

where d is the depth of the circumferential crack, and h is the oxide thickness. If one makes the assumption that the curvature of the circumferential crack is large compared to d, and neglects the modulus mismatch across the oxide-metal interface, the results of Ref. [37] indicate that $\psi = 0$ when $d = 2.7\ M/P$. As shown in Fig. 10b, if the crack deviates closer to the top free surface, the sign of the mode-II stress-intensity factor will drive it down. If the crack deviates closer to the oxide-metal interface, the sign of the mode-II stress-intensity factor will drive it up [37]. Therefore, this is the depth at which such a crack would propagate in a stable trajectory.

The results of these calculations are shown in Fig. 11 for different values of h. The intersection of the two lines shows the spall depth. For the case of an oxide thickness of 90 μm, the radial crack cannot propagate to the depth d_s corresponding to the mode-II = 0 plane in Fig. 11a, no matter how brittle the oxide is assumed to be (see Fig. 9a for the energy-release rate at a crack depth of d_s). So spalling would not occur for this thickness of oxide. On the other hand, the radial crack can grow below the possible spall depth if the oxide is thicker than about 100 μm for a toughness of about 100 J/m^2 (see Fig. 9b for the energy-release rate at the corresponding crack depth

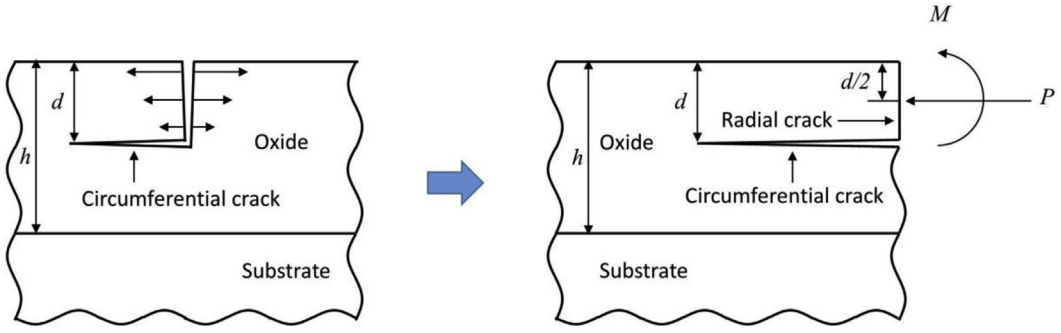

(a)

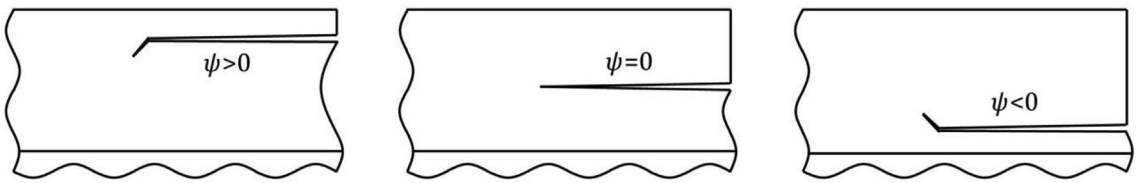

(b)

Fig. 10. **(a)** A circumferential crack parallel to the interface at depth d, intersecting with a radial crack where a representative effective load and moment is applied on the surface. **(b)** The effects of crack tip phase angle, ψ, on the crack trajectory.

of d_s in Fig. 11b). In this case, spalling can possibly occur. Conversely, Fig. 11c indicates that spalling can occur 19 μm above the metal-oxide interface for the 110 μm thick oxide even for a toughness as high as 600 J/m^2 (see Fig. 9c for the energy-release rate at the corresponding crack depth of d_s in Fig. 11c). We further verified that spalling is thermodynamically viable at the possible spall depths by calculating the corresponding energy-release rates [37]. The calculated depth of the spalls is above the metal-oxide interface, so they would leave a thin layer of oxide adhered to the metal, as is sometimes observed experimentally [10].

Finally, it is noted that experimental observations indicate the existence of periodic bands of high-porosity that develop in the oxide layer parallel to the metal-oxide interface [38]. These could result in a lower fracture toughness parallel to the interface than we have assumed, which would further enhance spalling by the phenomena proposed.

3.3. Effect of alloy composition of the cladding

The alloy composition, such as the level of tin in the cladding, can affect the oxidation and creep rate [39,40]. Here we provide a discussion on the effects of these rates to put our analysis in a broader perspective with regard to different claddings.

Cracking and spalling of the oxide layer are caused by the tensile circumferential stresses that develop in the oxide layer. These stresses come mostly from contact between the pellet and cladding. Simulations showed that similar levels of stress developed in thinner oxides with lower oxidation rates. This arises because the time for the pellet to contact the cladding is dictated by the pellet swelling rate and the cladding creep rate. Therefore, a lower oxidation rate leads to a thinner oxide layer at the time when contact occurs. Furthermore, the subsequent evolution of circumferential stresses is dictated by the swelling rate. Therefore, less oxide grows before the stresses reach a critical level. As a result, cracking tends to occur in a thinner oxide layer with lower oxidation rate. This can explain experimental observations of oxide delamination from advanced zirconium alloys (AXIOM) cladding at a relatively thin oxide thickness because of the lower oxidation rate [41].

The diffusional creep rate of the cladding depends on the composition and grain size. With a higher creep rate, the contact between pellet and cladding occurs sooner owing to faster creep-down of the cladding. Thus, a higher creep rate leads to an earlier development of tensile circumferential stresses within the oxide layer. Therefore, generally speaking, cracking and spalling occurs when the oxide is thinner, if the creep rate is higher.

4. Conclusion

A finite-element model to study the evolution of radial cracks in the oxide that lead to spalling under normal operating conditions was constructed by incorporating the multiple mechanisms of creep, swelling and oxidation. First, an analysis of the development of stresses in the oxide was conducted. Before contact occurs between the fuel pellet and cladding, the circumferential stress in the outer oxide layer is initially very compressive owing to growth stresses. This compression increases as the cladding creeps down to the pellet. However, volume expansion associated with newly formed oxide at the interface induces a tensile contribution to the stresses in the outer regions of the oxide formed earlier. Swelling of the fuel pellet after contact with the cladding further induces a strong tension in the oxide layer by pushing the cladding outward.

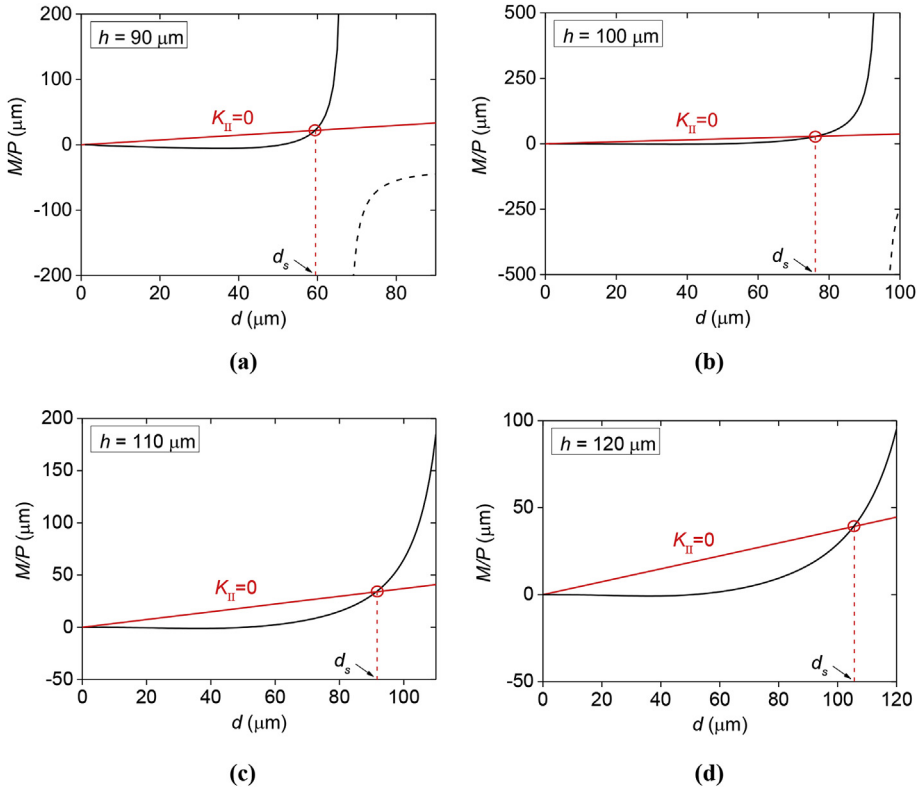

Fig. 11. Ratio of equivalent moment to force as a function of crack depth, d, at different oxide thicknesses: **(a)** 90 μm, **(b)** 100 μm, **(c)** 110 μm, and **(d)** 120 μm. The dotted portion of the line corresponds to depths at which $K_I < 0$, owing to the compressive stresses in the oxide. The straight line corresponds to the ratio required to make $K_{II} = 0$. The intersection between the two solid lines indicates a stable spall depth, d_s.

With the combined effects of these two phenomena, the circumferential stress in the outer region of the oxide becomes tensile after a critical thickness.

A cracking analysis in the oxide layer was performed by using the calculated values of the circumferential stress. The crack depth for crack channeling was determined by calculating the energy-release rate for extending radial cracks into the oxide. This analysis showed that energy-release rate increases dramatically as the oxide thickness increases. Subsequently, the steady-state energy-release rate for crack channeling was computed. The results indicated that this value also increases dramatically with oxide thickness. The results could be classified into three cases depending on the thickness and toughness of the oxide layer: (i) radial cracking without channeling, (ii) channel cracking within the oxide, and (iii) channel crack through the entire oxide and possibly penetrating into the metal. Corresponding spall depths were also calculated; these indicated that spalling will leave a thin oxide layer adhered to the metal, as occasionally observed experimentally.

As distinct from previous studies that have concentrated on oxide spalling under transient conditions comparable to RIA, the present study emphasizes spalling under normal operating conditions for PWRs. This gives an explanation for cracking of the oxide layer during service. A fuller extension could be developed by introducing the concept of periodic cracking.

Acknowledgements

This research was supported by the Consortium for Advanced Simulation of Light Water Reactors (http://www.casl.gov), an Energy Innovation Hub (http://www.energy.gov/hubs) for Modeling and Simulation of Nuclear Reactors under U.S. Department of Energy Contract No. DE-AC05-00OR22725.

References

[1] K. Une, S. Ishimoto, Dissolution and precipitation behavior of hydrides in Zircaloy-2 and high Fe Zircaloy, J. Nucl. Mater. 322 (2003) 66–72.
[2] A.M. Garde, G.P. Smith, R.C. Pirek, Effects of hydride precipitate localization and neutron fluence on the ductility of irradiated Zircaloy-4, Zircon, in: Nucl. Ind. Elev. Int. Symp, 1996, pp. 407–429. ASTM Int. ASTM STP 1295.
[3] A.T. Motta, L.Q. Chen, Hydride formation in zirconium alloys, JOM 64 (2012) 1403–1408.
[4] S. Arsene, J. Bai, P. Bompard, Hydride embrittlement and irradiation effects on the hoop mechanical properties of pressurized water reactor (PWR) and boiling-water reactor (BWR) Zircaloy cladding tubes: Part III. Mechanical behavior of hydride in stress-relieved annealed and recrystall, Metall. Mater. Trans. 34 (2003) 579–588.
[5] B. Cox, Pellet-clad interaction (PCI) failures of zirconium alloy fuel cladding—a review, J. Nucl. Mater. 172 (1990) 249–292.
[6] H.M. Chung, T.F. Kassner, Cladding metallurgy and fracture behavior during reactivity-initiated accidents at high burnup, Nucl. Eng. Des. 186 (1998) 411–427.
[7] F. Schmitz, J. Papin, High burnup effects on fuel behaviour under accident conditions: the tests CABRI REP-Na, J. Nucl. Mater. 270 (1999) 55–64.
[8] J. Papin, B. Cazalis, J.M. Frizonnet, J. Desquines, F. Lemoine, V. Georgenthum, F. Lamare, M. Petit, Summary and interpretation of the CABRI REP-Na program, Nucl. Technol. 157 (2007) 230–250.
[9] C. Vitanza, A review and interpretation of ria experiments, Nucl. Eng. Technol. 39 (2007) 591–602.
[10] J. Desquines, V. Georgenthum, F. Lemoine, B. Cazalis, The fracture and spallation of zirconia layers in high burnup PWR fuel claddings submitted to RIA transients, in: 18th Int. Conf. Struct. Mech. React. Technol. C. 3, 2005, pp. 444–453.
[11] V. Georgenthum, J. Desquines, V. Bessiron, Influence of outer zirconia transient cracking and spalling on thermomechanical behaviour of high burnup fuel rod submitted to RIA, J. Nucl. Sci. Technol. 43 (2006) 1089–1096.
[12] A.B. Johnson, E.R. Gilbert, R.J. Guenther, Behavior of spent nuclear fuel and storage system components in dry interim storage, PNL-4189, Prep. U. S. Dep. Energy under Contract DE-AC06-76RLO 1830, Pacific Northwest Lab, 1982.
[13] D. Rozzia, M. Adorni, A. Del Nevo, F.D. Auria, Capabilities of TRANSURANUS code in simulating power ramp tests from the IFPE database, Nucl. Eng. Des. 241 (2011) 1078–1086.
[14] N. Baba, Aspects of electrochemistry, chemistry, physics, and applications of "Less-Common Metals,", J. Less Common Met. 43 (1975) 295–301.
[15] Y. Kim, Y. Jeong, J. Jang, Stress measurements during thin film zirconium oxide growth, J. Nucl. Mater. 412 (2011) 217–220.
[16] C. Roy, G. David, X-ray diffraction analyses of zirconia films on zirconium and Zircaloy-2, J. Nucl. Mater. 37 (1970) 71–81.
[17] P. Platt, E. Polatidis, P. Frankel, M. Klaus, M. Gass, R. Howells, M. Preuss, A study into stress relaxation in oxides formed on zirconium alloys, J. Nucl. Mater. 456 (2015) 415–425.
[18] J. Godlewski, P. Bouvier, G. Lucazeau, L. Fayette, Stress distribution measured by Raman spectroscopy in zirconia films formed by oxidation of Zr-based alloys, Zircon. Nucl. Ind. Twelfth Int. Symp. ASTM Int. ASTM STP 1354 (2000) 877–900.
[19] A.T. Motta, A. Couet, R.J. Comstock, Corrosion of zirconium alloys used for nuclear fuel cladding, Annu. Rev. Mater. Res. 45 (2015) 311–343.
[20] E. Hillner, Corrosion of zirconium-base alloys—an overview, ASTM Int. ASTM STP 633 (1977) 211–235.
[21] E. Hillner, D.G. Franklin, J.D. Smee, Long-term corrosion of Zircaloy before and after irradiation, J. Nucl. Mater. 278 (2000) 334–345.
[22] H. Wang, Z. Hu, W. Lu, M.D. Thouless, A mechanism-based framework for the numerical analysis of creep in Zircaloy-4, J. Nucl. Mater. 433 (2013) 188–198.
[23] H.J. Frost, M.F. Ashby, Deformation Mechanism Maps: the Plasticity and Creep of Metals and Ceramics, Pergamon Press, 1982.
[24] M.J. Roddy, W.R. Cannon, G. Skandan, H. Hahn, Creep behavior of nanocrystalline monoclinic ZrO2, J. Eur. Ceram. Soc. 22 (2002) 2657–2662.
[25] A.H. Chokshi, Diffusion, diffusion creep and grain growth characteristics of nanocrystalline and fine-grained monoclinic , tetragonal and cubic zirconia, Scripta Mater. 48 (2003) 791–796.
[26] D.M. Owen, A.H. Chokshi, The high temperature mechanical characteristics of superplastic 3 mol% yttria stabilized zirconia, Acta Mater. 46 (1998) 667–679.
[27] L.J. Siefken, E.W. Coryell, E.A. Harvego, J.K. Hohorst, SCDAP/RELAP5/MOD 3.3 code manual: MATPRO—a library of materials properties for light-water-reactor accident analysis, Idaho Natl. Eng. Environ. Lab. (2001).
[28] M.S. Hu, M.D. Thouless, A.G. Evans, The decohesion of thin films from brittle substrates, Acta Metall. 36 (1988) 1301–1307.
[29] J.L. Beuth, Cracking of thin bonded films in residual tension, Int. J. Solid Struct. 29 (1992) 1657–1675.
[30] A. Bravo-Leon, Y. Morikawa, M. Kawahara, M.J. Mayo, Fracture toughness of nanocrystalline tetragonal zirconia with low yttria content, Acta Mater. 50 (2002) 4555–4562.
[31] J. Kondoh, H. Shiota, K. Kawachi, T. Nakatani, Yttria concentration dependence of tensile strength in yttria-stabilized zirconia, J. Alloy. Comp. 365 (2004) 253–258.
[32] B. MUSSLER, M.V. Swain, N. Claussen, Dependence of fracture toughness of alumina on grain size and test technique, J. Am. Cermaic Soc. 65 (1982) 566–572.
[33] M.D. Thouless, Cracking and delamination of coatings, J. Vac. Sci. Technol. 9 (1991) 2510–2515.
[34] M.D. Thouless, E. Olsson, A. Gupta, Cracking of brittle films on elastic substrates, Acta Metall. Mater. 40 (1992) 1287–1292.
[35] J.W. Hutchinson, Z. Suo, Mixed mode cracking in layered materials, Adv. Appl. Mech. 29 (1991) 63–191.
[36] V.B. Shenoy, A.F. Schwartzman, L.B. Freund, Crack patterns in brittle thin films, Int. J. Fract. 109 (2001) 29–45.
[37] M.D. Thouless, A.G. Evans, M.F. Ashby, J.W. Hutchinson, The edge cracking and spalling of brittle plates, Acta Metall. 35 (1987) 1333–1341.
[38] P. Bossis, D. Pecheur, K. Hanifi, J. Thomazet, M. Blat, Comparison of the high burn-up corrosion on M5 and low tin Zircaloy-4, J. ASTM Int 3 (2006) 1–32.
[39] A.M. Garde, S.R. Pati, M.A. Krammen, G.P. Smith, R.K. Endter, Corrosion behaviour of Zircaloy-4 cladding with varying tin content in high temperature pressurised water reactors, Zircon. Nucl. Ind. ASTM STP 1245 (1994) 760–778.
[40] G. Sabol, R.J. Comstock, R. Weiner, P. Larouere, R. Stanutz, In-reactor corrosion performance of ZIRLO and Zircaloy-4, Zircon, in: Nucl. Ind. Tenth Int. Symp, 1994, pp. 724–744. ASTM STP 1245.
[41] A.M. Garde, G. Pan, A.J. Mueller, L. Hallstadius, Oxide surface peeling of advanced zirconium alloy cladding after high burnup irradiation in pressurized water reactors, in: Zircon. Nucl. Ind. 17th Int. Symp, 2015, pp. 1–20. ASTM STP 1543.